Supporting Information

Linking in-situ charge accumulation to electronic structure in doped $SrTiO_3$ reveals new design principles for hydrogen evolving photocatalysts

Benjamin Moss[1,2], Qian Wang[3,4], Keith T. Butler[5], Ricardo Grau-Crespo[6] Shababa Selim[1,2], Anna Regoutz[7], Takashi Hisatomi[8], Robert Godin[1,9], David J. Payne[10], Andreas Kafizas[1,11], Kazunari Domen[6,12], Ludmilla Steier[1*] and James R. Durrant[1,2]

[1] Department of Chemistry, Imperial College London, London, W12 0BZ, UK
[2] Centre for Plastic Electronics, Imperial College London, Prince Consort Road, London SW7 2BZ, UK
[3] Department of Chemical System Engineering, School of Engineering, The University of Tokyo, 7-3-1 Hongo, Bunkyo-ku, Tokyo 113-8656, Japan
[4] Department of Chemistry, University of Cambridge, Lensfield Road, Cambridge CB2 1EW, UK

[5] SciML, Scientific Computing Division, Rutherford Appleton Laboratory, Harwell, OX11 0QX, UK
[6] Department of Chemistry, University of Reading, Whiteknights, Reading, RG6 6AD, UK

[7] Department of Chemistry , University College London, 20 Gordon Street, London, WC1H 0AJ, UK
[8] Research Initiative for Supra-Materials, Interdisciplinary Cluster for Cutting Edge Research, Shinshu University, 4-17-1 Wakasato, Nagano-shi, Nagano 380-8553, Japan
[9] Department of Chemistry, University of British Columbia, Kelowna, BC, V1V 1V7, Canada
[10] Department of Materials, Imperial College London, London, SW7 2AZ, UK
[11] Grantham Institute, Imperial College London, London, SW7 4AZ, UK
[12] Office of University Professor, The University of Tokyo, 7-3-1 Hongo, Bunkyo-ku, Tokyo 113-8656, Japan
* correspondence to: l.steier@imperial.ac.uk

I. Methods

Synthesis of Rh and La,Rh:SrTiO$_3$: Rh:SrTiO$_3$ and La,Rh:SrTiO$_3$ were synthesised by a previously reported two step solid state reaction.[1] In the first step, rutile TiO$_2$ (Kanto Chemicals, 99.0%) and SrCO$_3$ (Kanto Chemicals, 99.9%, calcined in air at 573 K for 1 h) were ground in a mortar to obtain a mixture with a Sr/Ti ratio of 1.05. The mixture was then calcined at 1423 K for 10 h to produce SrTiO$_3$. In the second step, SrTiO$_3$ was ground in ethanol with Rh$_2$O$_3$ (Kanto Chemicals, 99.9%) and calcined at 1373 K for 6 h to make Rh:SrTiO$_3$. For La,Rh:SrTiO$_3$ fabrication, both La$_2$O$_3$ (Kanto Chemicals, 99.99%, freshly calcined in air at 1273 K for 12 h) and Rh$_2$O$_3$ (Kanto Chemicals, 99.9%) were calcined at 1373 K for 6 h. In both cases, La and Rh were added such that the nominal doping concentration (i.e [Rh]/([Rh]+[Ti] or [La]/([La]+[Sr]) was 4 mol%. H$_2$-Rh:SrTiO$_3$ was produced by annealing Rh:SrTiO$_3$ powder at 573 K in a hydrogen atmosphere for two hours. For transient absorption scavenger studies, films were fabricated directly from powders by dispersing 50 mg of powder in water, drop casting on to glass and calcining at 673 K for 1 h.

Fabrication of photocatalyst sheets: (La),Rh:SrTiO$_3$ photocatalyst sheets were fabricated by a modified particle transfer method. The procedure was identical to previous reports[1,2] except that Mo:BiVO$_4$ particles were omitted and a much thicker Au layer (ca. 2 μm as opposed to ca. 350 nm) was used to create a continuously conductive back contact. Doped SrTiO$_3$ (20 mg) was suspended in isopropanol (99.9%, 0.5 ml), drop-cast on a glass substrate (3×3 cm^2) and left to dry at room temperature overnight. The Au back contact was then deposited by thermal vacuum evaporation (VFR-200M/ERH, ULVAC KIKO) at an evaporation rate of approximately 20 nm s^{-1} at a base pressure of 2.6×10^{-3} Pa. The exposed Au surface was then bonded to a second glass plate (3×3 cm^2) with double sided carbon tape and lifted off the primary glass plate. The resulting photocatalyst sheet was then ultrasonicated twice in distilled water for 2 minutes to remove any unattached particles.

Scanning electron microscopy (SEM): SEM images were taken on a LEO GEMINI 1525 microscope using a 1.5 keV electron beam and a secondary electron detector. As the back Au contact in the photocatalyst sheets provides a highly conductive pathway for charge, no conductive coating was required. EDX was performed on the same instrument using an Oxford Instruments X-act detector at a beam voltage of 20 keV and a 60 mm aperture.

X-ray photoelectron spectroscopy (XPS): XPS was performed on a Thermo Scientific K-alpha+ instrument. Powdered samples were attached to a stainless-steel plate using conductive carbon tape. The instrument uses monochromated and microfocused Al Kα (hν = 1486.6 eV) radiation to eject photoelectrons which are then analysed using a 180° double-focusing hemispherical analyser with a 2D detector. Spectra were collected at 2x10^{-9} mbar base pressure. A flood gun was used to minimize sample charging. All samples were referenced against the C-C peak of adventitious carbon in the C 1s spectrum at a binding energy of 284.8 eV to correct for any charge that is not neutralised by the flood gun. Further effects were then accounted for by taking the separation from the O 1s oxide peak. Data was analysed using the CASA XPS package.

Ultraviolet-visible absorption spectroscopy and spectroelectrochemistry: Reflectance spectra of the photocatalyst sheets were collected using a Shimadzu UV-vis 2600 spectrophotometer equipped with an integrating sphere, using a disk of pressed barium sulphate as a 100% reflecting reference. The resulting diffuse reflectance spectra were then converted to a unit proportional to absorptance using the Kubelka-Munk function, $F(R) = \frac{k}{s} = \frac{(1-R)^2}{(2R)}$. Where *k* and *s* respectively correspond to absorption and scattering coefficients and *R* corresponds to the reflectance (the fraction of light reflected in comparison to the fully scattering BaSO$_4$ reference). For spectroelectrochemical measurements, photocatalyst sheets were measured in a quartz cuvette in three-electrode configuration using an

Ag/AgCl (sat'd KCl) reference electrode, a platinum mesh counter electrode and the doped $SrTiO_3$ working electrodes in 0.1 M Na_2SO_4 electrolyte (pH 7). Potentials were applied using a Metrohm Autolab PGSTAT 101 potentiostat. Reflection and refraction from the cuvette do not change with applied potential and so did not contribute to the observed change in the Kubelka-Munk function. A small offset at 820 nm is visible due to a change in detector and a low background level of reflected light in this experiment.

Hybrid density functional calculations: All calculations are performed using the VASP package.[3] For doping calculations a 3x3x3 supercell was created. In the case of co-doping all symmetry inequivalent positions of the dopants were explored, although no qualitative and very little quantitative differences were found. We therefore use a single configuration for presenting our results. For relaxation of atomic positions the PBEsol functional[4], projector augmented pseudopotentials[5], and a cut-off energy of 500 eV, with k-point sampling defined as an evenly spaced grid in reciprocal space with a density scaled to the unit cell size were used to achieve uniform sampling with a target length cut-off of 10 Å, as described by Moreno and Soler[6]. The relaxed structures were then used for input to hybrid DFT calculations using the HSE06 functional[4] to calculate accurate electronic structure.

Diffuse reflectance transient absorption and photoinduced absorption: Transient and photoinduced absorption measurements were carried out on a home built setup described in our previous publications.[7] Briefly, micro-second to second transient absorption decays were acquired by measuring the diffuse reflectance of the opaque samples studied herein. A Nd:YAG laser (OPOTEK Opolette 355 II, 7 ns pulse width) was used as the excitation source, producing 355 nm light that was transmitted to the sample using a liquid light guide. An excitation power density of 400 μJ/cm^2 was typically used in conjunction with a laser repetition rate of 0.8 Hz. Probe light was generated by a 100 W Bentham IL1 quartz halogen lamp. Long pass filters (Comar Instruments) and an IR filter (H_2O, 5 cm path length) were positioned between the lamp and sample to minimise short wavelength irradiation and heating of the sample. Diffuse reflectance from the sample was collected and relayed to a monochromator (Oriel Cornerstone 130) through a long pass filter to select the probe wavelength. Acquisitions were triggered by a photodiode (Thorlabs DET10A) exposed to laser scatter. A Si photodiode (Hamamatsu S3071) was used as a detector in the visible region and an InGaAs diode (Hamamatsu G10899-03K) in the near IR. Data at times faster than 2 ms were amplified by custom electronics and recorded by an oscilloscope (Tektronics DPO3012) while data slower than 2 ms was simultaneously recorded on a National Instrument DAQ card (NI USB-6251). Kinetic traces were typically obtained from the average of 100 laser pulses. Data was acquired and processed using software written in the LabVIEW environment (Austin Consultants). Photoinduced absorption data, were collected with the same setup replacing the laser pulse by a continuous wave illumination of a 365 nm LED at an intensity of 8 mW cm^{-2}, corresponding to ½ sun of absorbed photons assuming a sharp absorption edge at 470 nm. The percentage change in reflectance was calculated according to

pioneering work by Wilkinson and co-workers.[8] Here the fractional change in reflected light due to transient absorption is:

$$R_t = \frac{V_t - V_0}{V_0}$$

Where V_0 is the voltage arising on Si photodiode from the probe beam before the pump, V_t is the voltage on the diode at time *t* after the pump. The % change in absorption (% *Abs.)* is thus:

$$\%\, Abs = (1 - R_t) \cdot 100$$

The changes of reflectance observed were low, with the largest signals being on the order of 1%. This enabled the transient signal to be taken as directly proportional to the concentration of excited state species. [9]

II. Supporting Figures

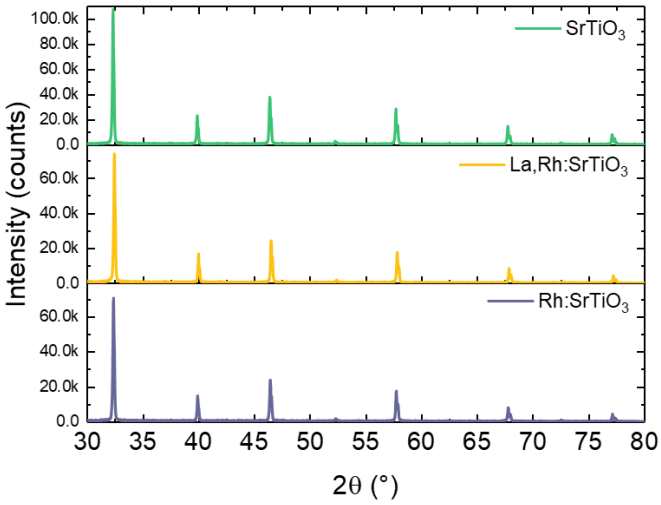

Figure S0 XRD patterns of the materials studied in this work.

S1. Ground state reflectance spectra.

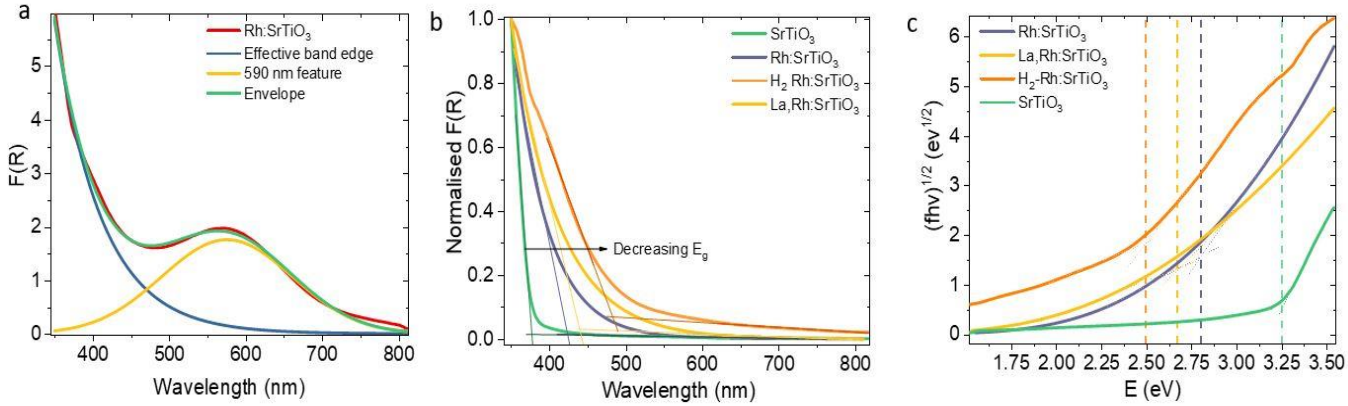

Figure S1. **Ground state reflectance spectra.** (a) Fitted absorption spectra and envelope for $Rh:SrTiO_3$. (b) Absorption spectra for $SrTiO_3$, $Rh:SrTiO_3$, H_2-$Rh:SrTiO_3$, and $La,Rh:SrTiO_3$ after subtraction of the 500-800 nm absorption feature (c) Band gap assessment using the a modified Tauc method for scattering materials proposed by Chen and Miller for the analysis of bandgaps with a scattering background.[10]

In order to separate the effective band edge from the absorption tail of the 500-800 nm feature (peaking at 590 nm), the absorption profile was approximated with an envelope composed of an exponential (effective band edge) and a gaussian function (500-800 nm feature). This process is shown in Figure S1a. By subtracting the gaussian profile from the absorption spectrum, an approximate profile for the band edge absorption spectrum can be obtained (Figure S1b). This shows consecutive decreases in the effective band gap upon (i) Rh doping (ii) chemical reduction of Rh, either by co-doping or reduction in a hydrogen atmosphere. This trend is reflected in the indirect band gap (Figure S1c), determined using a modified Tauc method proposed by Chen and Miller for use in strongly scattering materials.[10] The slightly wider band gap for $La,Rh:SrTiO_3$ is attributed to a small fraction of Rh^{4+} likely segregated in the core of the particles, and is beyond the scope of this study.

S2. X-ray photoelectron spectroscopy analysis.

Comparison of C 1s, Sr 3p, O 1s and Ti 2p, Rh 3d core level and valence band photoelectron spectra

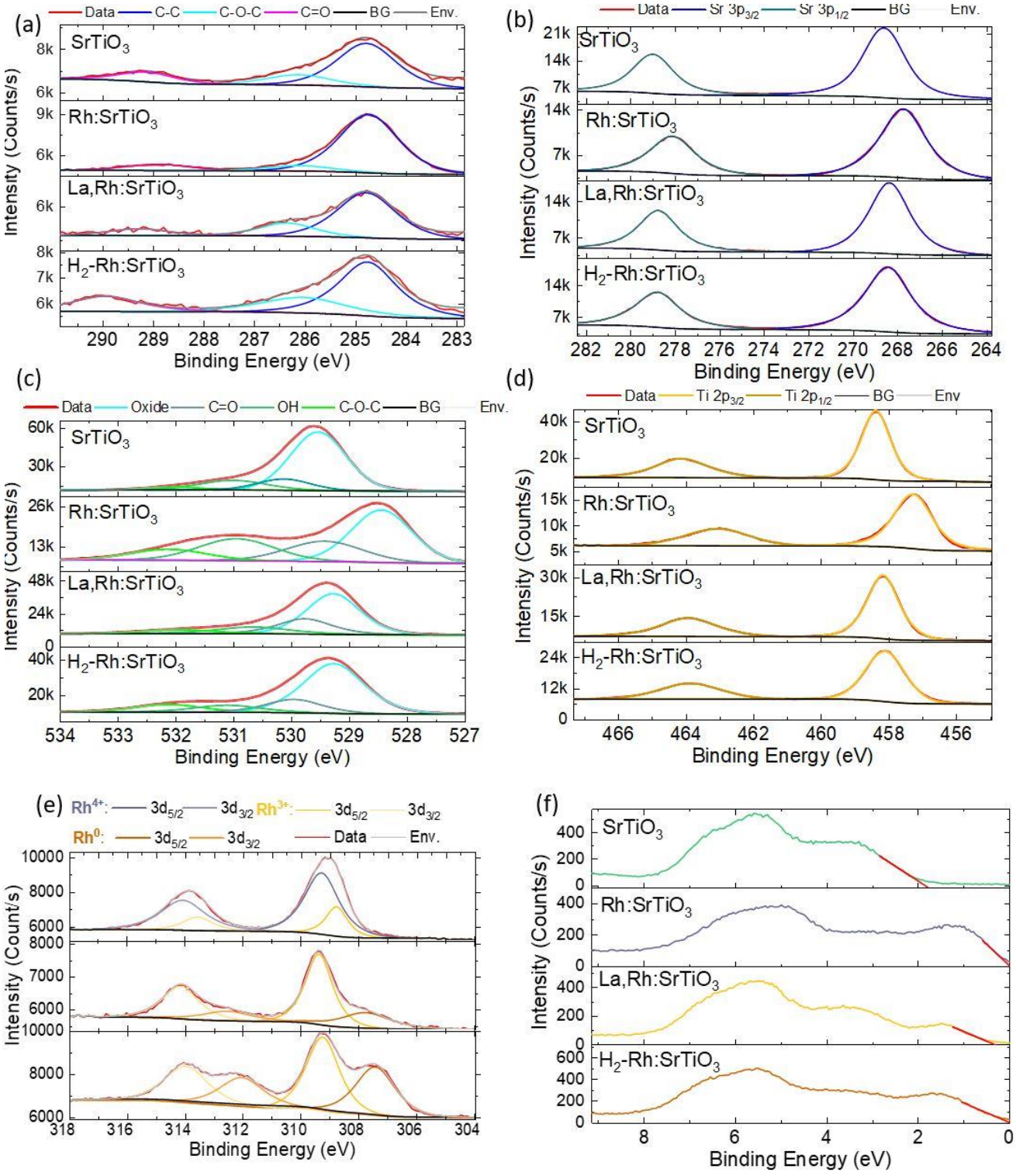

***Figure S2.1* X-ray photoelectron spectroscopy analysis.** Comparison of the C1s (a), Sr 3p (b), O 1s (c), Ti 2p (d), Rh 3d (e) core level spectra of $SrTiO_3$, Rh:$SrTiO_3$, La,Rh:$SrTiO_3$ and H_2-Rh:$SrTiO_3$. Fitted component spectra, the envelope from resulting from the fitting procedure as well as the background used (Shirley) is shown alongside the raw data. (f) Valence band photoelectron spectra of the materials. A linear fit of the valence band maximum region (red) is used to estimate the valence band-Fermi level separation.

C 1s

Figure S2.1a compares the C 1s core level spectra for the materials studied herein. Three adventitious carbon environments are clearly observed in the C 1s spectrum of all samples. The largest component at lowest binding energy was assigned to C-C type environments and referenced to 284.8 eV to correct the binding energy scale for charging of the sample. Due to the shift in the binding scale that is observed in the other core lines for doped samples, individual scans were checked for a shift indicative of an accumulation of charge during the experiment. No such effect was observed, implying that the shifts seen herein are not due to strong charging/poor grounding of the samples and the correction at 284.8 eV is valid. The remaining higher binding energy environments were assigned to adventitious C-O-C (c.a. 286.1 eV) and C=O groups (c.a. 289.1 eV) using a systematic study of carbon environments by Siegbahn and co-workers as a reference.[11] Carbon residues can arise the contamination of surfaces in air or from the reaction of the $SrTiO_3$ with carbon in the air, leading to a $SrCO_3$ enriched surface.[12] This distinction (physisorbed surface carbon residues vs chemisorbed carbonate) is beyond the scope of this work, however, it is likely that both occur, with both adventitious residues and a carbonate enriched surface present in variable quantities depending on the sample preparation method.[12]

Sr 3p

The Sr 3p spectra of the samples (Fig. S2.1b) shows a doublet consistent with peak ratios of c.a. 2:1, consistent with a single Sr^{2+} environment split by spin orbit coupling into $3p_{3/2}$ and $3p_{1/2}$ components The spin orbit splitting of around 10.3 eV between the peaks the compares well to the literature.[13] A 1 eV shift to lower binding energy is observed in $Rh:SrTiO_3$, as well as a smaller downshift observed for $La,Rh:SrTiO_3$, $H_2:Rh:SrTiO_3$. An identical shift is also observed in the O 1s and Ti 2p spectra. This indicates a shift in the entire binding energy scale between samples and is addressed in more detail in Supplementary Figure S2.2.

O 1s

A minimum of four components were required for a good fit of the O 1s spectra (Fig. S2.1c) if full width half maximum of the components are to be constrained to an empirically reasonable range for metal oxides.[14] Using the results of a systematic study of the O 1s environments of metal oxides and hydroxides by Levasseur and co-workers as a reference[14], the largest component (c.a. 529.5 eV) is assigned to O^{2-} (i.e oxide) groups that make up the bulk of $SrTiO_3$. Two of the remaining three groups are assigned to oxidised adventitious carbon (C=O at c.a. 530.1 eV and C-O at c.a. 532.0 eV). The, broader intermediate peak (c.a. 531.0 eV) is assigned either to surface OH[14] For doped samples, these peaks were shifted to higher binding energy due to Fermi level effects discussed Supplementary Figure S2.2.

Ti 2p

The Ti 2p spectra (Fig. S2.1d) shows a reasonable fit to a single doublet with a 2p 3/2:1/2 peak ratio of c.a. 2:1, consistent with a single Ti^{4+} environment predominating, split by spin orbit coupling into $2p_{3/2}$ and $2p_{1/2}$ components. The spin orbit splitting of around 5.7 eV compares well with the literature.[13] Again, doped samples show the same environments but shifted to higher binding energies by the same amount as other core lines, indicative of a shift in the entire binding energy scale rather than a true chemical shift of Ti states (see Supplementary Figure S2.2).

Rh 3d

A more complex picture is observed in the Rh 3d spectra (Supporting Fig S2.1e). As with the other spectra, a shift in the binding energy scale occurs, however, this effect is counteracted by changes in oxidation states of Rh that occurs between samples. This makes assignment of oxidation states impossible without first decoupling the chemical shifts from Fermi level effects. The final results of this analysis are discussed here (see supplementary Fig. S2.2 for discussion of decoupling, and S2.3. for assignment of oxidation states). Table S1 summarises the surface Rh concentration observed (i.e. [Rh]/([Rh]+[Ti])) as well oxidation states observed in all materials. Surface Rh concentrations exceeding the nominal doping concentration expected from the stoichiometry of the solid-state reaction (4 mol%) were observed in all powders. Similar effects have been observed in previous studies both TiO_2 and $SrTiO_3$ which have been doped Rh by solid state reaction[15–17] and is attributed to the surface segregation of Rh. Such 'core-shell' structures, typical of materials doped through solid state reaction, have previously been observed in this material[15] as well as analogous Rh doped TiO_2 systems[16] and explains the different intensities of colour observed between the materials despite identical nominal doping concentrations. DFT calculations (Fig. S6.5) indicate that adjacent Rh states do not strongly interact. Consequently, the energies and degree of localisation of Rh 4d states at higher Rh concentrations is similar to that of lower concentrations (i.e. for Rh^{4+} localised states at the effective VB maximum and a localised state in the mid-gap). Rh:$SrTiO_3$, Rh primarily adopts the 4+ oxidation state at the surface with 80% adopting the 4+ of Rh state and 20% adopting the 3+ state. This is attributed to the reductive influence of oxygen vacancies in the lattice. Consistent with the concept, Rh^{4+} is further reduced by hydrogen reduction as H_2-Rh:$SrTiO_3$ is composed of 56 % Rh^{3+} and 44 % Rh^0. Consistent with the reductive effect of La co-doping, Rh primarily adopts the 3+ oxidation state in La,Rh:$SrTiO_3$ (75%) with a minority of states as Rh^0. This is again attributed to the presence of oxygen vacancies within the lattice, which would be expected to further reduce Rh^{3+} states induced by La co-doping.

Consistent with the reductive effect of La co-doping, Rh primarily adopts the 3+ oxidation state in La,Rh:$SrTiO_3$ (75%) with a minority of states as Rh^0. This is again attributed to the presence of oxygen vacancies within the lattice, which would be expected to further reduce Rh^{3+} states induced by La co-doping. Rh^0 has a measurable effect on both initial transient amplitude and the density of charge that accumulates in PIA (see discussion of Fig S 5.7a,b). However, Rh^0 has no significant effect on the kinetics of Rh:$SrTiO_3$ and La,Rh:$SrTiO_3$ in our slow timescale TAS studies and does not seem to act as a catalyst on the surface of La,Rh:$SrTiO_3$ as electrons are accumulated over a period of several tens of seconds. Only Rh^{4+} appears to produce a vacant mid gap state which determines if CB electrons can accumulate. Additional, more subtle effects which effect the density of CB electrons may arise from different proportions of Rh^0 and Rh^{3+}, merit further study as optimising the system to avoid the formation of Rh^0 states may further enhance efficiency.

Table S1 **Rh compositions and oxidation states measured by XPS.**

Sample	$SrTiO_3$	Rh:$SrTIO_3$	La,Rh:$SrTiO_3$	H_2-Rh:$SrTiO_3$
Surface [Rh] (mol %)	0	20	6	20
Surface [Rh^{4+}] (%)	0	80	0	0
Surface [Rh^{3+}] (%)	0	20	75	56
Surface [Rh^0] (%)	0	0	25	44
Surface [La^{3+}] (%)	0	0	6	0

Valence band spectra

Figure S2.1f shows VB photoelectron spectra of the samples studied. Here, a complex interplay of effects is also observed. Upon Rh doping, filled Rh 4d states are introduced above the $SrTiO_3$ VB. This is accompanied by a shift to p-type conductivity, which shifts the entire binding energy scale lower binding energy (compare envelopes of $SrTiO_3$ and Rh:$SrTiO_3$ in Fig. S2.1). The results of separating these factors can be found in Figure 3 in the main text and S2.3b below.

In undoped $SrTiO_3$, a valence band – Fermi Level separation of 1.8 eV was estimated using the intercept of a linear function fitted the decay of the valence band (shown in red). A similar analysis gives intercepts of 0.1 eV for Rh:$SrTiO_3$ and H_2:Rh:$SrTiO_3$ and 0.3 eV for La,Rh:$SrTiO_3$.

Decoupling Fermi level effects from the spectrum using a relative binding energy scale

In S2.1, the photoelectron spectra of differently doped sampled are offset with respect to one another by the same amount regardless of the core line chosen. For example, the left-hand side of Figure S2.2a compares the photoelectron spectra of the oxide component of the O 1s spectrum and the Ti $2p_{3/2}$ spectrum for undoped, Rh doped and La,Rh co-doped $SrTiO_3$. A 1 eV shift to lower binding energy is observed upon Rh doping in both the Ti and O peaks, with a smaller analogous shift observed in La,Rh:$SrTiO_3$. However, the separation of the peaks (indicated by Δ) remains constant. As it is highly unlikely that this shift is the result of identical chemical shifts for both O^{2-} and Ti^{4+}, we attribute these changes to a downward shift in the Fermi level position upon doping shifting all peaks to lower binding energy. Further evidence for this effect is provided by the equation in Figure S2.2a, which predicts that the difference in binding energy between two peaks should be independent of the position of the Fermi level.[16] Re-plotting the binding energy scale as the difference in energy with respect to the O 1s oxide peak leads to an alignment of the Ti 2p spectra (right hand side of Fig. 3b), consistent with the single (Ti^{4+}) environment this is observed. The Fermi level induced misalignment of the binding energy scale between the samples identified here affects the entire binding energy scale, including the VB region, and prevents direct comparison of the energies of Rh states using the absolute binding energy (E_B) scale.[17] By re-potting VB data, relative energies of filled Rh 4d states above the $SrTiO_3$ VB can be compared (Fig. S2.2b).

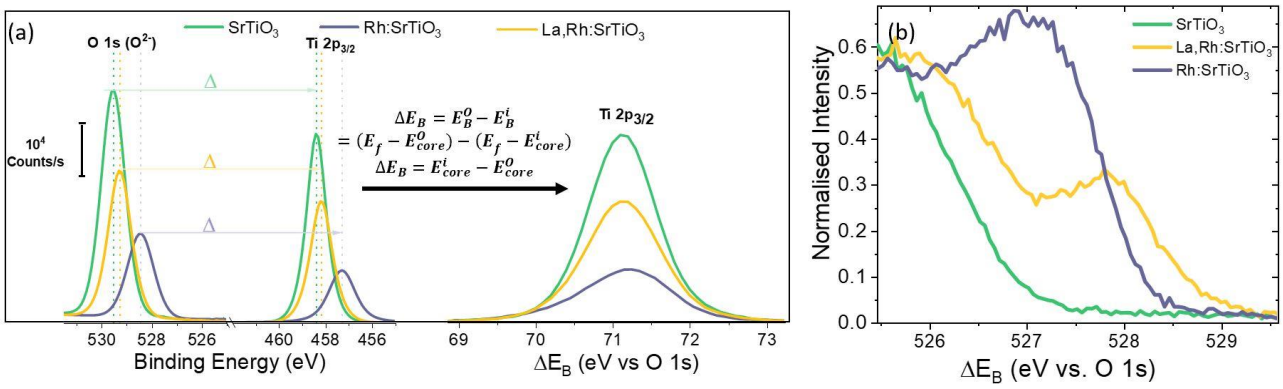

Figure S2.2 **Introduction of the relative binding energy scale.** *(a)* Left hand side: The O^{2-} (oxide) component of the O 1s spectrum and Ti 2p (e.g $2p_{3/2}$) spectra shift to lower binding energies by identical amounts upon doping. Consequently, the O^{2-} - Ti 2p peak separation (Δ) is invariant upon doping. This can be explained by the equation in the centre of the panel which shows that, for a given material, referencing the binding energy of one core line against another produces a property that is insensitive to the position of the Fermi level. Symbols: E_B^i is the binding energy of a peak of interest (here Ti $2p_{3/2}$), E_B^O is the binding energy of O^{2-} in the O 1s spectrum, E_{core}^i and E_{core}^O correspond to the absolute energy of these states. Right hand side: the alignment of Ti $2p_{3/2}$ component spectra plotted on the ΔE_B scale (referenced against the O^{2-}) demonstrates that the E_B scales are misaligned due to differences in Fermi level position. (b) VB spectra comparing the Rh 4d states introduced above the $SrTiO_3$ valence band on the ΔE_B scale.

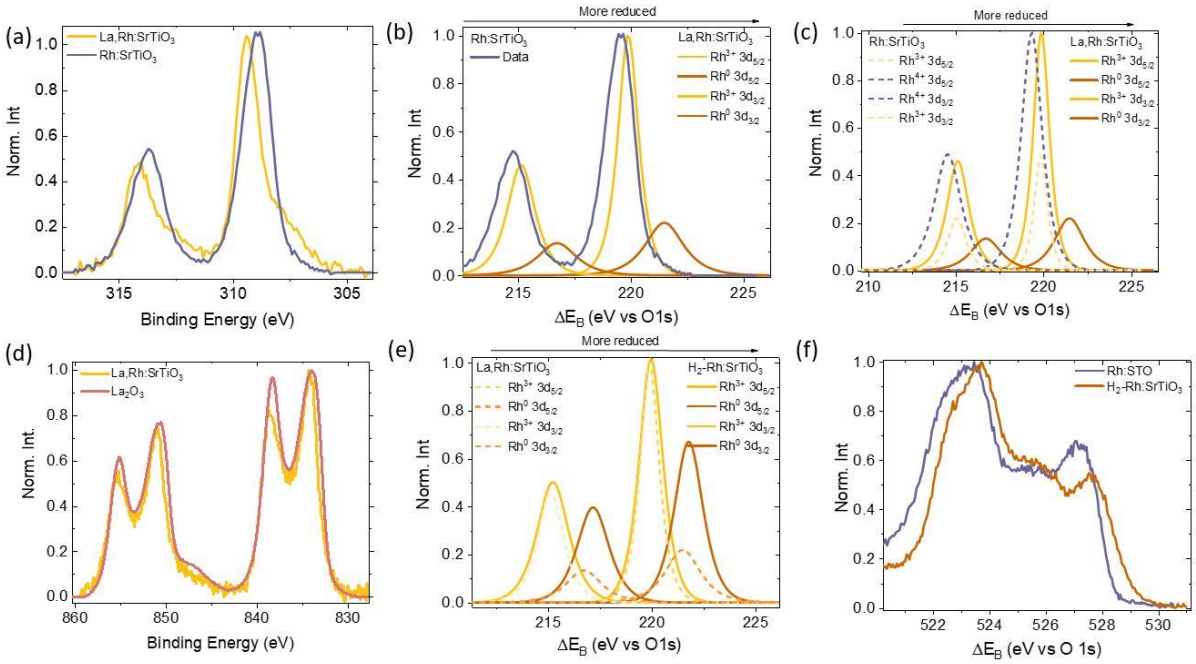

***Figure S2.3* X-ray photoemission analysis using the relative binding energy scale.** (a) Raw Rh 3d photoemission spectra of $Rh:SrTiO_3$ plotted on a binding energy scale. (b) Rh 3d component spectra for $La,Rh:SrTiO_3$ plotted alongside the raw Rh 3d core level spectrum of $Rh:SrTiO_3$ on the ΔE_Bscale. (c) Rh 3d component spectra for both materials plotted on the ΔE_Bscale. (d) La 3d spectrum of $La,Rh:SrTiO_3$, plotted alongside a La_2O_3 reference measured on the same instrument. (e) Comparison of the Rh 3d component spectra of $La,Rh:SrTiO_3$ and H_2-$Rh:SrTiO_3$ on the ΔE_Bscale. (f) Comparison of the valence band spectra of $Rh:SrTiO_3$ and H_2-$Rh:SrTiO_3$ on the ΔE_Bscale.

Rationale for the assignment of Rh oxidation states and the effect of hydrogen reduction on the valence band spectrum.

Figure S2.3a compares the raw Rh 3d spectra of $Rh:SrTiO_3$ to that of $La,Rh:SrTiO_3$ on the binding energy scale. The spectrum of $Rh:SrTiO_3$ is significantly broader than that of $La,Rh:SrTiO_3$. In the $Rh:SrTiO_3$ spectrum a slight asymmetry towards lower binding energy is observed with a peak at lower binding energy than in $La,Rh:SrTiO_3$. The spectrum of $La,Rh:SrTiO_3$ clearly exhibits two environments, one with a peak falling at higher binding energy than the $Rh:SrTiO_3$ maximum and another to lower binding energy. This counter intuitive result (where an apparently more reduced material has a peak at higher binding energy than its more oxidised counterpart) can be attributed to differences in Fermi level position between the two samples (Fig S2.2a). Using the Δ_{EB} scale decouples chemical shifts arising from changes in the oxidation state of Rh and Fermi level effects. Comparison of the spectrum of the raw $Rh:SrTiO_3$ spectrum to the two doublet components of $La,Rh:SrTiO_3$ on the ΔE_B scale (Fig. S2.3b) resolves this conundrum, as here, the peak maximum of $La,Rh:SrTiO_3$ falls 0.3 eV higher than $Rh:SrTiO_3$ (note: higher ΔE_B corresponds to lower Rh binding energy assuming that the nature of O^{2-} does not change upon doping [16]).

Figure S2.3c shows a comparison of the two fitted doublet components that are clearly discernible in $La,Rh:SrTiO_3$ with the raw spectrum of $Rh:SrTiO_3$ on the ΔE_B scale. The more oxidised doublet component of $La,Rh:SrTiO_3$ matches the envelope shape of $Rh:SrTiO_3$ at higher ΔE_B values, but is substantially narrower. This strongly suggests the presence of two environments under the envelope of $Rh:SrTiO_3$. Comparison of two component doublets of $Rh:SrTiO_3$ to those in $La,Rh:SrTiO_3$ (Fig. S2.3c) shows the envelope of $Rh:SrTiO_3$ to be made up of a larger doublet at lower ΔE_B and a smaller doublet matching with the more oxidised component which predominant component of $La,Rh:SrTiO_3$. Based on the common oxidation states of Rh as an oxide (+4 and +3) as well as a previous XPS study of Rh doped $SrTiO_3$ films grown epitaxially by pulsed laser deposition,[18] these components are assigned to

Rh^{4+} and Rh^{3+} respectively. The most reduced component of La,Rh:$SrTiO_3$ is assigned to Rh^0, based again on a study of epitaxially grown Rh:$SrTiO_3$. The reduction of Rh^{4+}, predominantly to Rh^{3+}, in La,Rh:$SrTiO_3$ is consistent with an ionic charge compensation mechanism as La is observed in the 3+ oxidation state in La,Rh:$SrTiO_3$ (similar multiplet splitting to La_2O_3 in Fig. S2.2d) with a 1:1 Rh:La ratio (i.e 6 mol % La).

Comparison of H_2-Rh:$SrTiO_3$ to La,Rh:$SrTiO_3$ (Fig. S2.3e) shows broadly similar components with differing Rh^{3+}:Rh^0 ratios. As expected, a similar effect on the valence band to La co-doping (Figure 2b in main text and S2.2b) is observed Rh^{4+} reduction using hydrogen annealing with the effective valence band edge shifting to higher energy upon Rh reduction (Fig. S2.3f). This is consistent with a change in the orbital structure of Rh rather than La orbital contribution near the band edges (see following sections and main text).

S3. EDX mapping

(a) (b)

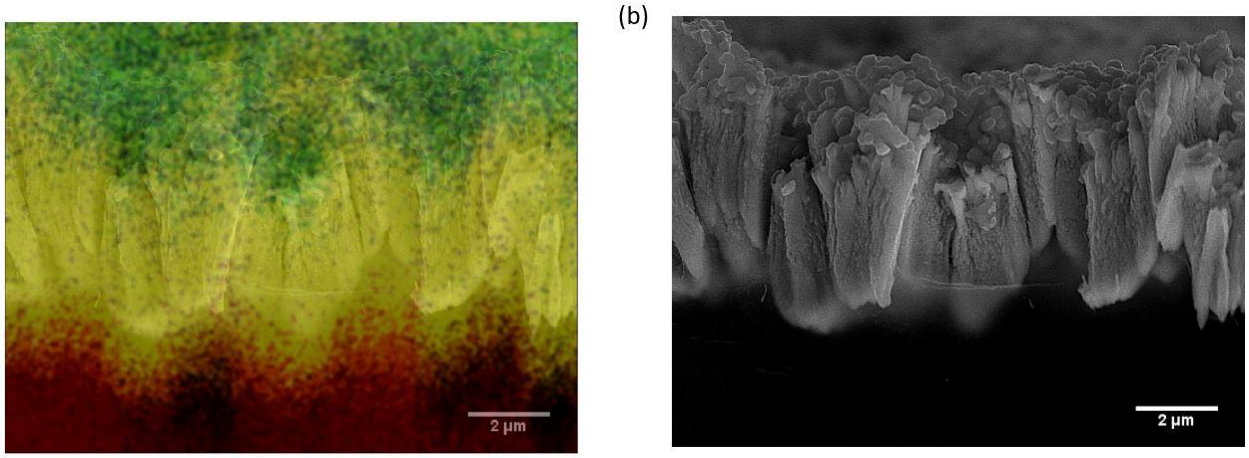

Figure S3. **EDX mapping of La,Rh:$SrTiO_3$ photocatalyst sheet half electrode.** *a)* Spatially resolved energy dispersive X-ray emission analysis superimposed on b) a cross-sectional SEM image of a photocatalyst sheet half electrode. X-ray emission from the particle layer is caused by Ti and Sr (green/blue). Particles are embedded in Au (yellow). Red corresponds to x-ray emission from the carbon tape substrate.

S4. Spectroelectrochemistry and cyclic voltammetry

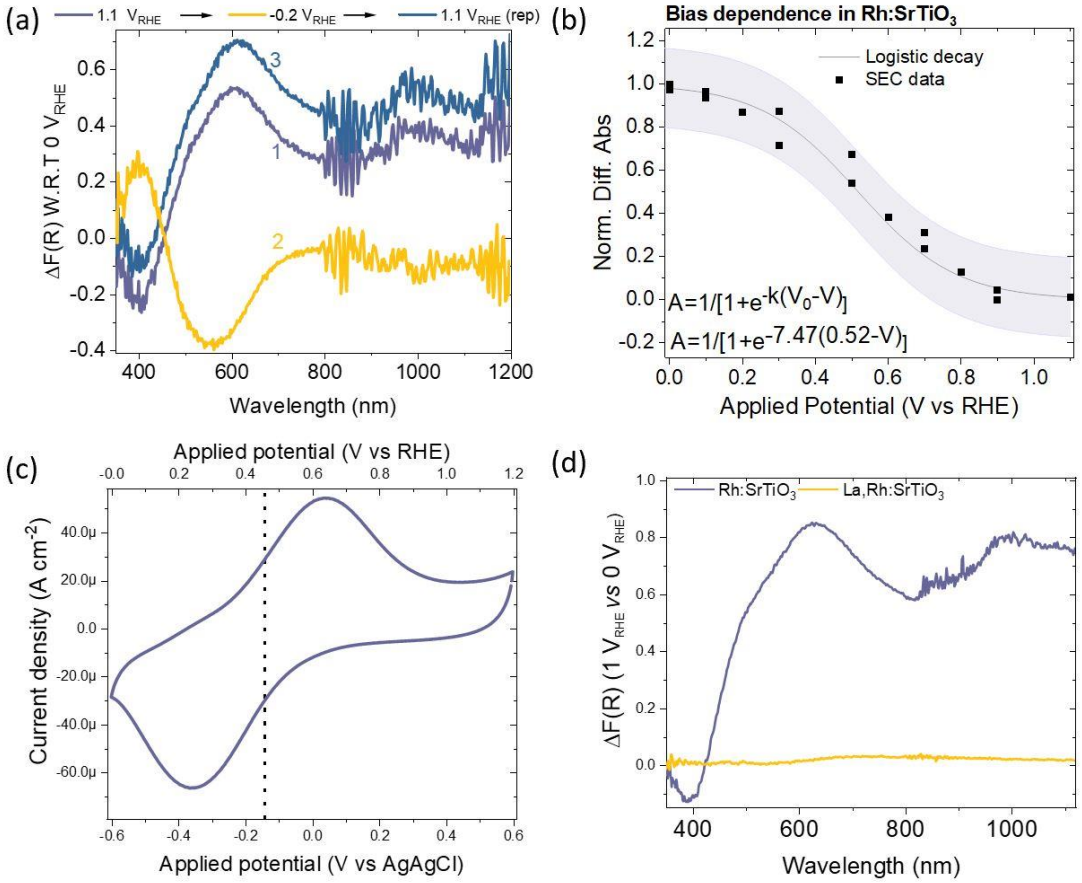

Figure S4. **Spectroelectrochemical and cyclic voltammetry measurements.** (a) Reversibility of the optical response to applied potential of a Rh:$SrTiO_3$ photocatalyst sheet. In order to visualise spectra at both positive and negative potentials, spectra are plotted with respect to a reference spectrum at 0 V_{RHE}. (b) Normalised SEC response of Rh:$SrTiO_3$ photocatalyst sheets to applied potential. Here 620 nm ground state bleach is monitored, with the maximum bleaching at 0 $_{VRHE}$ normalised to 1 (conditions 0.1 M Na_2SO_4, pH 7). This data was found to fit to a sigmoidal function with a midpoint of 0.52 V_{RHE} (c) Cyclic voltammogram of a Rh:$SrTiO_3$ photocatalyst sheet with a half wave potential of 0.46 V_{RHE}. (d) Comparison of the Maximum SEC change (i.e. 1 V_{RHE} vs 0 V_{RHE}) observed in (La),Rh:$SrTiO_3$ photocatalyst sheets. (conditions 0.1 M Na_2SO_4, pH 7)

S5. Assignment of time resolved optical spectra.

To understand the effect of doping on the transient spectrum of $SrTiO_3$, scavenger studies were performed on $SrTiO_3$ and La,Rh:$SrTiO_3$ to distinguish the spectral features related to photogenerated electrons.

Consistent with its much lower reactivity, electron scavengers had no clear effect on the transient spectra or kinetics of Rh:$SrTiO_3$. When hole scavengers (i.e. sacrificial electron donors) were employed, an irreversible colour change from purple to yellow was observed in Rh:$SrTiO_3$ – consistent with a change in the properties of the sample as Rh^{4+} becomes reduced. Consequently, scavengers could not be used to resolve the components of the transient spectrum of this material. Rather, assignments are made by comparison of the spectra of Rh:$SrTiO_3$ at positive and negative applied potential to those of La,Rh:$SrTiO_3$ and study of the intensity dependence of transient kinetics.

Assignment of the TA spectrum $SrTiO_3$

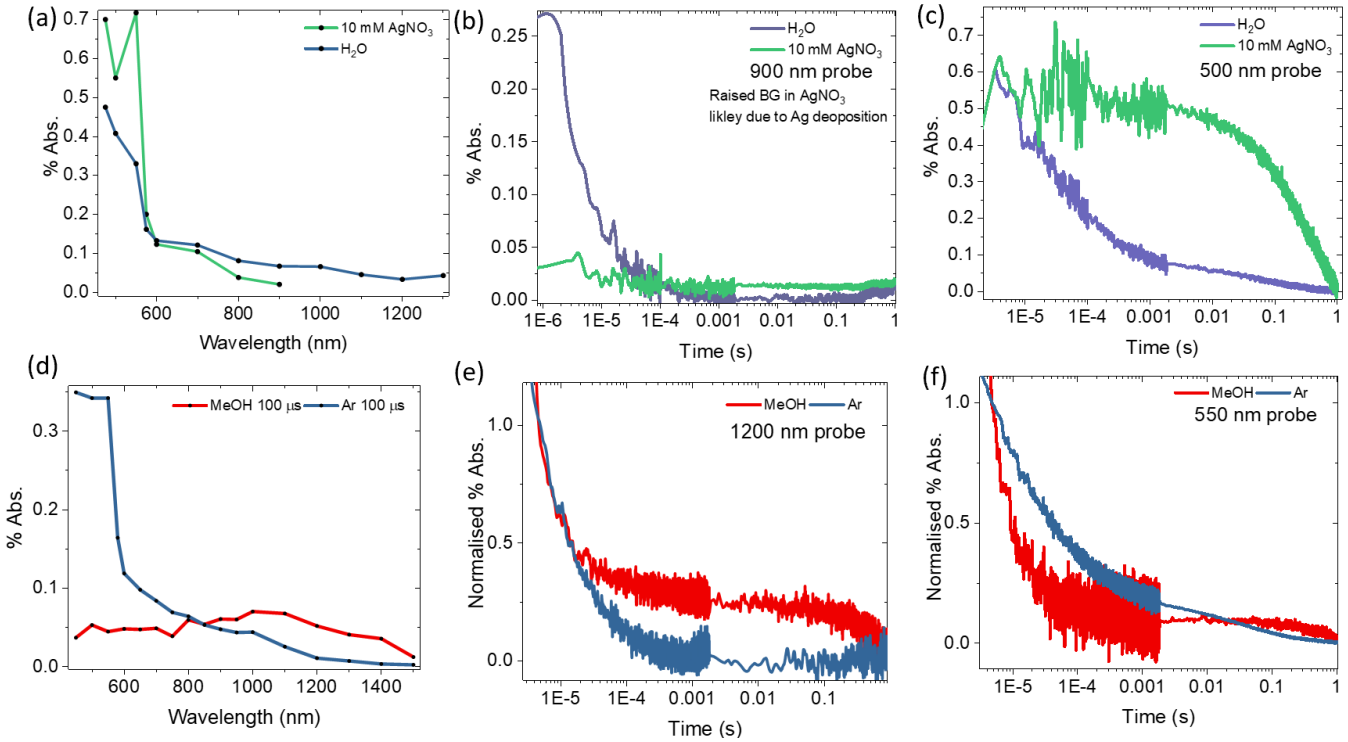

Figure S5.1 **Transient absorption spectroscopy measurements on $SrTiO_3$ nanoparticle films.** (a) Effect 10 mM $AgNO_3$ solution on the transient spectrum of $SrTiO_3$ (measured at 10 µs). Accompanying kinetics for these conditions at 900 (b) and 500 nm (c). (d) Effect of MeOH on the transient spectrum $SrTiO_3$ shown alongside transient kinetics for these conditions measured at 1200 nm (e) and 550 nm (f). (conditions 0.1 M Na_2SO_4, pH 7)

To aid in assignment of the transient absorption of photogenerated electrons in La,Rh:$SrTiO_3$, we began by attempting to resolve the absorption components of undoped $SrTiO_3$. Experiments were performed using electron and hole scavengers (i.e. sacrificial electron acceptors/donors) to ambiguously assign the spectrum, as the former should decrease electron lifetime and amplitude due to reaction, whilst the latter should increase electron lifetime and amplitude due to a decrease in the population of photogenerated holes available to recombine with photogenerated electrons.

Figures S5.1a-c show the effect of introducing $AgNO_3$ (an electron scavenger) on the transient spectrum and kinetics of $SrTiO_3$. In comparison to the control measurement (water) an increased transient absorption was observed at wavelengths <600 nm, whilst a decrease in absorption was observed in the NIR (>750 nm). Due to the strong scavenging effect, resulting formation of metallic Ag (which scatters in red/NIR) wavelengths > 900 nm could not be measured for this sample. However, transient kinetics at 900 nm (Fig. S5.1b) shows a complete loss of amplitude at or before the timescale of the experiment (c.a. 10 µs). This effect is consistent with complete reaction of electrons at times $\leq 10\mu s$. Further evidence of electron scavenging can be found from monitoring the transient kinetics at 500 nm. Here, a more persistent signal with increased amplitude is observed from 10 µs onwards in comparison to the control. This is consistent the absorption of photogenerated holes which remain after scavenging.

To confirm this assignment, we carried out a study of the effect of MeOH (a hole scavenger) on the transient spectrum and kinetics of $SrTiO_3$ (Fig. S5.1d-f). Here, the opposite effect to Ag^+ is observed in the transient spectrum, with a loss of amplitude at <600 nm and an increase in the NIR, leading to a broad flat spectrum in MeOH (Fig. S5.1d). As expected, more persistent transient signals are observed in the NIR (Fig. S5.1e) and faster decaying signals are observed at wavelengths < 600 nm (Fig. S5.1f).

The former is consistent a larger population of more slowly decaying photogenerated electrons, whilst the latter indicates the reaction of photogenerated holes with MeOH. Based on these results, we conclude that in undoped $SrTiO_3$ photogenerated electrons absorb predominantly in the NIR, and further (based on Fig. 5.1d) absorb exclusively at wavelengths > 1200 nm.

Assignment of the TA spectrum of La,Rh:$SrTiO_3$

Scavenger studies of La,Rh:$SrTiO_3$ (Fig. S5.2a-c) show similar results to those observed in undoped $SrTiO_3$ (Fig. S5.1a-c). Comparison of the transient spectrum of $AgNO_3$ to a water control (Fig. S5.2a) leads to an increased amplitude at wavelengths < 600 nm and decreased amplitude at wavelengths > 600 nm, most prominently in the NIR. Transient kinetics in $AgNO_3$ appear faster in the NIR (Fig. S5.2b) and slower at wavelengths <600 nm (Fig. S5.2c), concordant with the assignment of electrons in the NIR and holes <600 nm. These results indicate that, like undoped $SrTiO_3$, photogenerated electrons can again be monitored in the NIR. This is consistent with the results of DFT, which show the conduction band to be unchanged by doping.

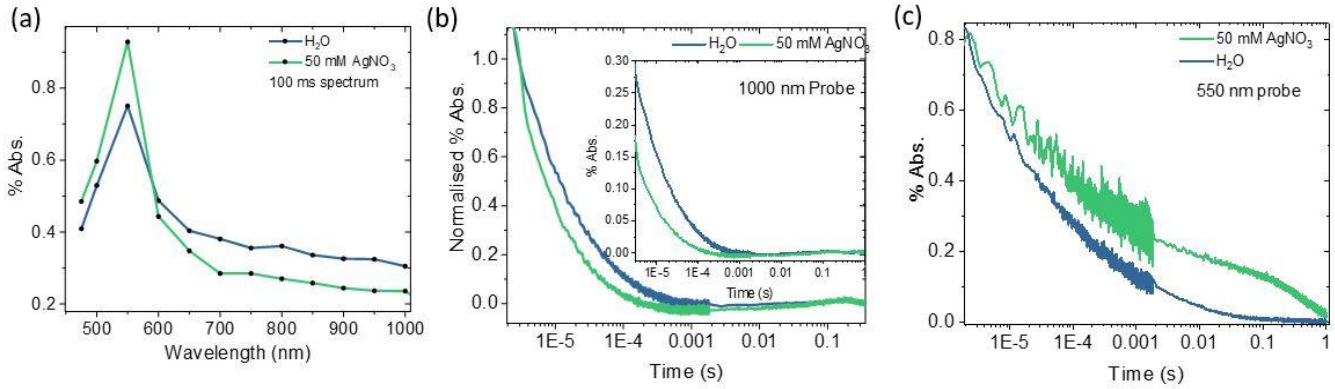

***Figure S5.2*. Transient absorption spectroscopy measurements on La,Rh:$SrTiO_3$ nanoparticle films.** Effect of 50 mM $AgNO_3$ on the transient spectrum (a) and transient kinetics of La,Rh:$SrTiO_3$, measured at 1000 nm (b) and 500 nm (c). Measured in 0.1 M Na_2SO_4, pH 7.

Additional supporting transient kinetics of (La),Rh:SrTiO$_3$ photocatalyst sheets.

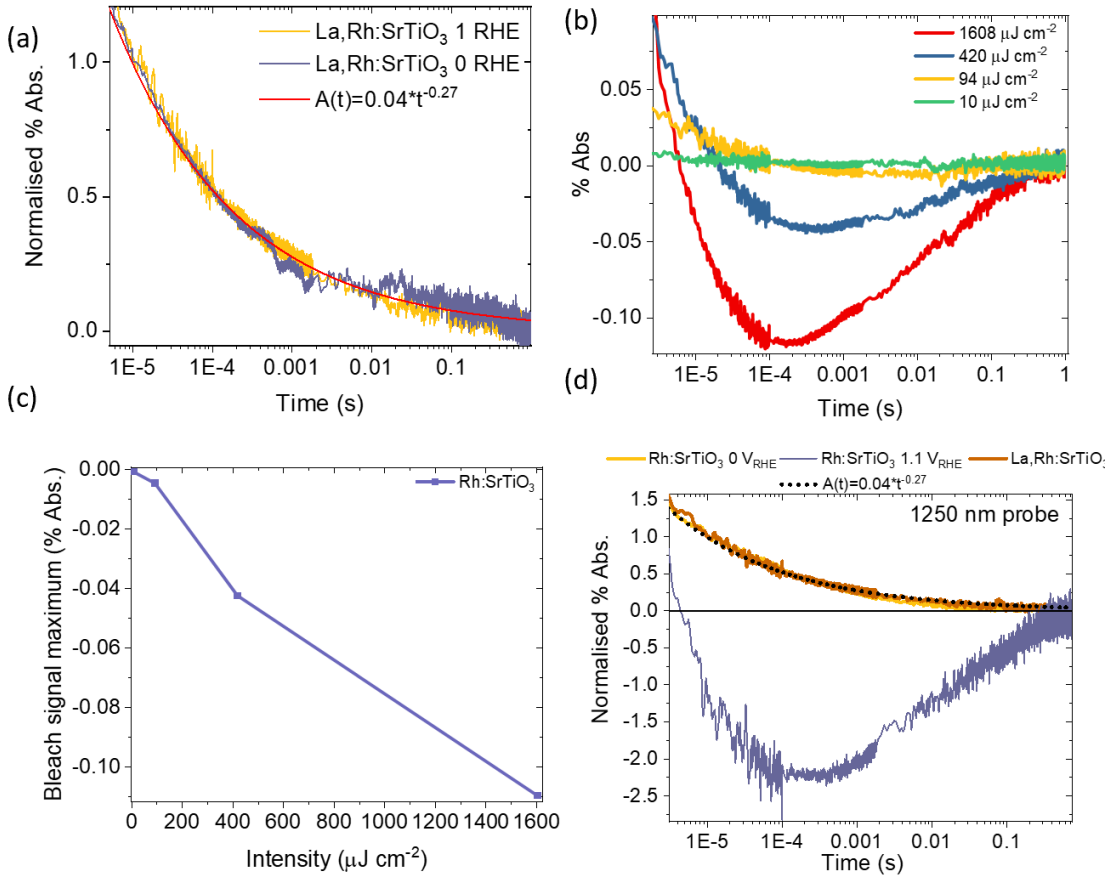

***Figure S5.3* Transient absorption spectroscopy measurements on photocatalyst sheet half-electrodes.** (a) Effect of applied potential on the transient electron kinetics (1250 nm) of La,Rh:SrTiO$_3$, showing identical transient kinetics at all applied potentials and decay dynamics fitting a power law function. (b) Intensity study of the 1250 nm bleach in Rh:SrTiO$_3$ measured at open circuit in 0.1 M Na_2SO_4 (pH 7) (c) Maximum bleaching amplitude from (b) as a function of intensity, showing a linear dependence. (d) Transient electron kinetics of Rh:SrTiO$_3$ at 0 V_{RHE} are identical to those observed for La,Rh:SrTiO$_3$ (a). At 1 V_{RHE} distinct kinetics dissimilar to La,Rh:SrTiO$_3$ are observed. (conditions 0.1 M Na_2SO_4, pH 7)

Note on the intensity dependence of the ground state bleach observed in Rh:SrTiO$_3$:

Figure S5.3b,c shows the intensity dependence of the broad bleach observed from 1100 nm onwards (probed at 1250 nm). A linear density on the maximum bleaching signal is observed. This suggests a trap density exceeding the number of carriers generated by a single laser flash (a maximum of c.a. 10^{19} photons cm^{-3}) - consistent with the high concentration of Rh^{4+} states in the system at positive applied potentials (c.a. 10^{20}-20^{21} cm^{-3})

Assignment of the TA spectrum Rh:SrTiO$_3$ photocatalyst sheets at negative potentials

Figure S5.4a shows the transient spectrum of Rh:SrTiO$_3$ as a function of applied potential**.** *The spectral shape of Rh:SrTiO$_3$ at negative potential is nearly identical to that of La,Rh:SrTiO$_3$* (Fig. S5.4b). Due to the identical spectral and kinetic behaviour (at 1250 nm, Fig. S5.3d) of Rh:SrTiO$_3$ to La,Rh:SrTiO$_3$ we

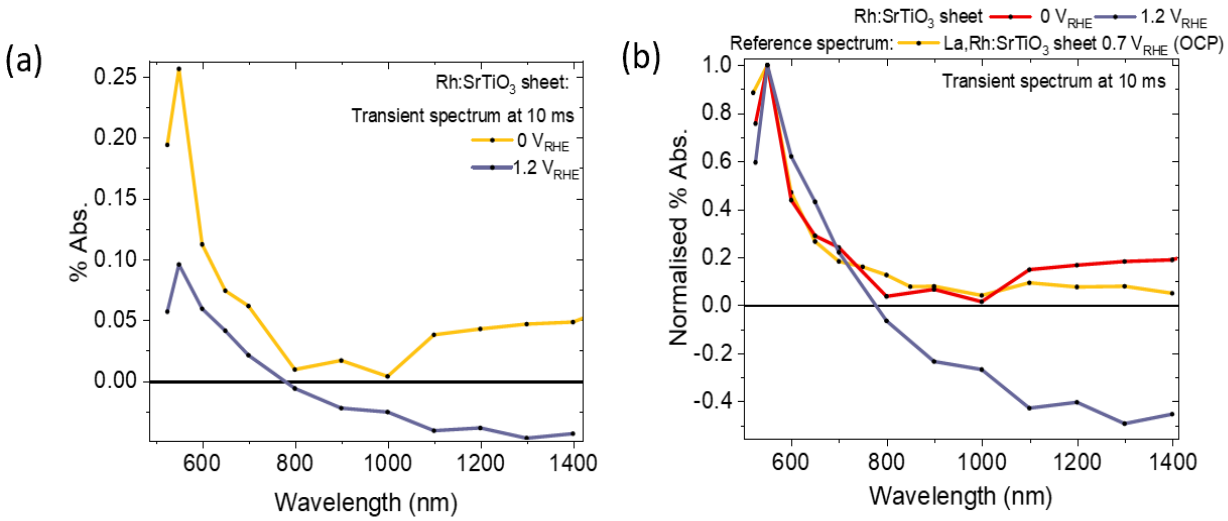

***Figure S5.4* Assignment of the TA spectrum Rh:$SrTiO_3$ photocatalyst sheets at negative potentials.** (a) The effect of applied potential on the transient spectrum of Rh:$SrTiO_3$ photocatalyst sheets, measured at 10 ms. (b) Comparison of the TA spectra in (a) to that of La,Rh:$SrTiO_3$ shows strong similarity at negative potentials. As with the transient kinetics, the spectrum of Rh:$SrTiO_3$ at positive potentials is dissimilar to La,Rh:$SrTiO_3$. (conditions 0.1 M Na_2SO_4, pH 7)

assign absorption at this potential, identically to La,Rh:$SrTiO_3$ – i.e. to photogenerated electrons near the CB. We note that bleaching around 600 nm is also predicted by SEC. However, this feature overlaps with the larger, positive hole absorption features. It is thus only after 800 nm, where hole absorption tapers off that bleaching from this feature is observed.

PIA spectra of (La),Rh:$SrTiO_3$ photocatalyst sheets.

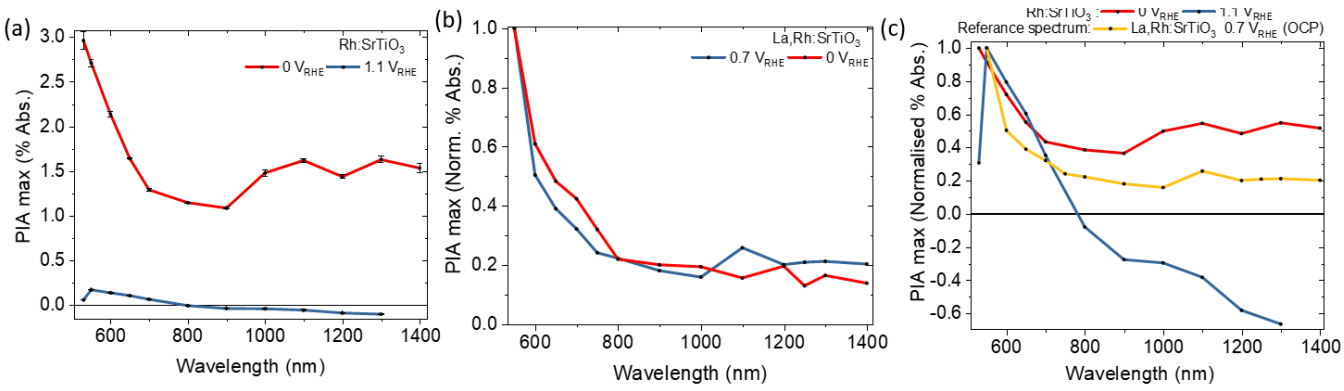

***Figure S5.5* PIA spectra of (La),Rh:$SrTiO_3$ photocatalyst sheets.** (a) Effect of applied potential on the PIA spectrum of Rh:$SrTiO_3$ photocatalyst sheets (conditions 0.1 M Na_2SO_4, pH 7). (b) Effect of applied potential on the PIA spectrum of La,Rh:$SrTiO_3$ sheets. (c) Comparison of the PIA spectra of Rh:$SrTiO_3$ and La,Rh:$SrTiO_3$ sheets show similar spectra when negative potentials are applied to Rh:$SrTiO_3$. As with S5.3 and S5.4 dissimilarity is observed when positive potentials are applied to Rh:$SrTiO_3$. (conditions 0.1 M Na_2SO_4, pH 7)

Reactivity of photogenerated electrons in La,Rh:$SrTiO_3$ under operational conditions.

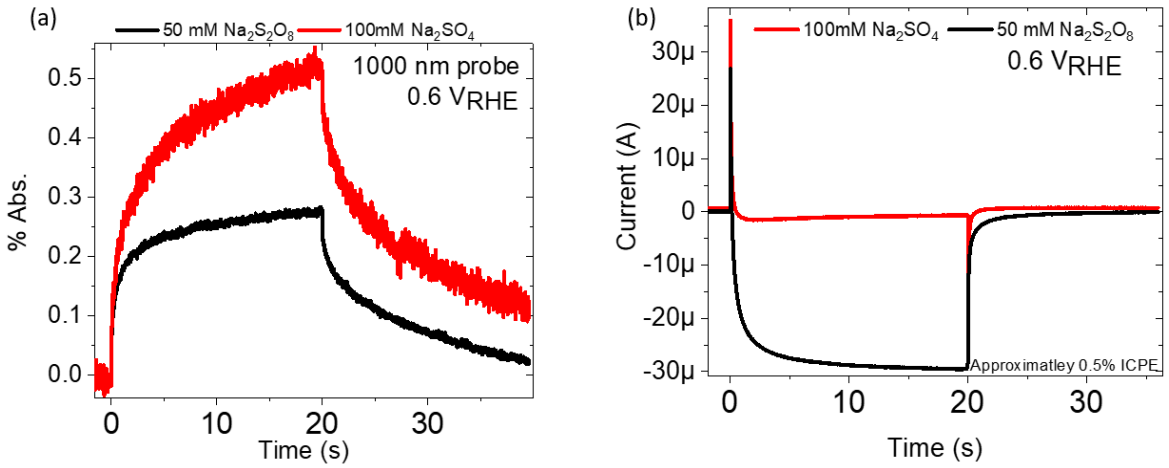

***Figure S5.6*. Effect of electron scavenger.** (a) The effect of $Na_2S_2O_8$ on the photoinduced absorption of electrons in La,Rh:$SrTiO_3$. (b) Photocurrent extracted during the measurement.

To better understand the reactivity of electrons accumulated in La,Rh:$SrTiO_3$, we employed $Na_2S_2O_8$, the reduction products of which are colourless (unlike $AgNO_3$). Figure S5.6a shows the effect on optical absorption of photogenerated electrons in La,Rh:$SrTiO_3$ photocatalyst sheets. Upon addition of $Na_2S_2O_8$, PIA signals with smaller amplitudes are observed. These signals decay more rapidly, consistent with the reaction of photogenerated electrons with a scavenger leading to a negative photocurrent (b). This indicates that photogenerated elections can be found on the surface of the particles and are available for reaction.

Effect of Rh^0 on charge carrier dynamics.

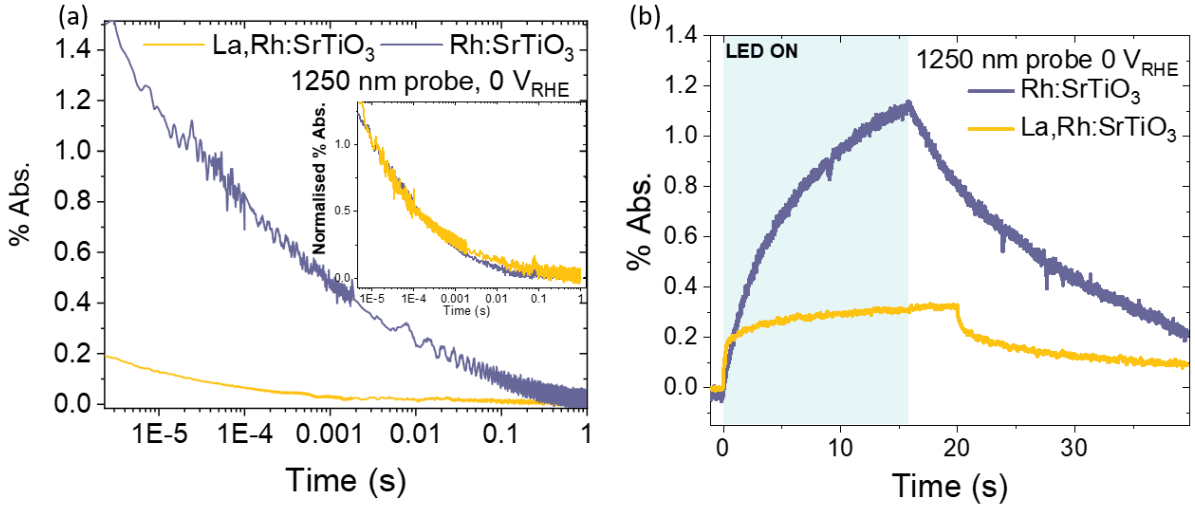

***Figure S5.7* Effect of Rh^0 on charge carrier dynamics.** (a) Comparison of the TA (a) and PIA (b) kinetics of La,Rh:$SrTiO_3$ and Rh:$SrTiO_3$ sheets at 0 V_{RHE}. The inset of (a) compares normalised kinetics.

Figure S5.7a compares the transient absorption of La,Rh:$SrTiO_3$ and Rh:$SrTiO_3$ sheets at 0 V_{RHE}. A 7.5-fold difference in initial amplitude between the two electrodes, however, both decay with identical kinetics (inset). This implies that recombination before the timescale of the experiment is more predominant in La,Rh:$SrTiO_3$. This effect is also visible in the PIA (Figure S5.7b). Here, the position of the quasi-equilibrium between generation and recombination under continuous wave illumination

shifted towards recombination in La,Rh:$SrTiO_3$ leading to a smaller population of photogenerated electrons. The principle difference between Rh:$SrTiO_3$ and La,Rh:$SrTiO_3$ at this potential is the presence of Rh^0 states in La,Rh:$SrTiO_3$. Metallic states are well known to act as recombination sites. Consequently, the 6-fold difference in electron population in PIA is attributed to the effect of Rh^0. Although the effect of modulating $Rh^{3+/0}$ population is significant, and will likely effect photocurrents in La,Rh:$SrTiO_3$, the effect of modulation the $Rh^{3+/4+}$ population presented in the main body of this paper is predominant as this dictates if CB electrons or mid gap trapped electrons are observed in PIA – as Rh:$SrTiO_3$ at positive applied potentials cannot accumulate CB electrons.

S6. Density Functional Theory Calculations.

Effect of doping on the $SrTiO_3$ frontier bands.

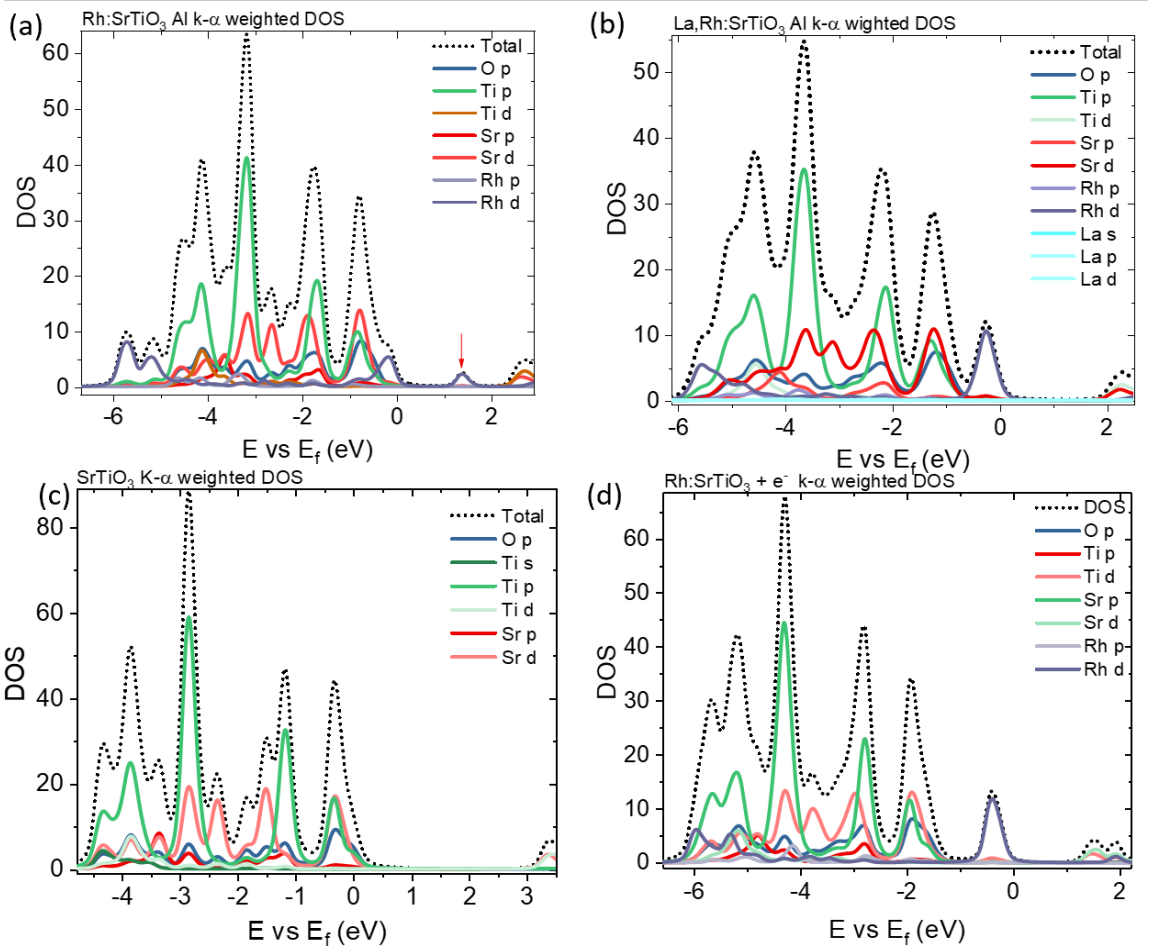

Figure S6.1. **Effect of doping on the $SrTiO_3$ frontier bands.** Calculated density of states (DOS) of (a) Rh:$SrTiO_3$, (b) La,Rh:$SrTiO_3$, (c)$SrTiO_3$, and (d) Rh:$SrTiO_3$ with an added electron in the presence of a positive compensating background charge. For comparison to XPS, all data is weighted by the relevant elemental x-ray absorptions cross sections.

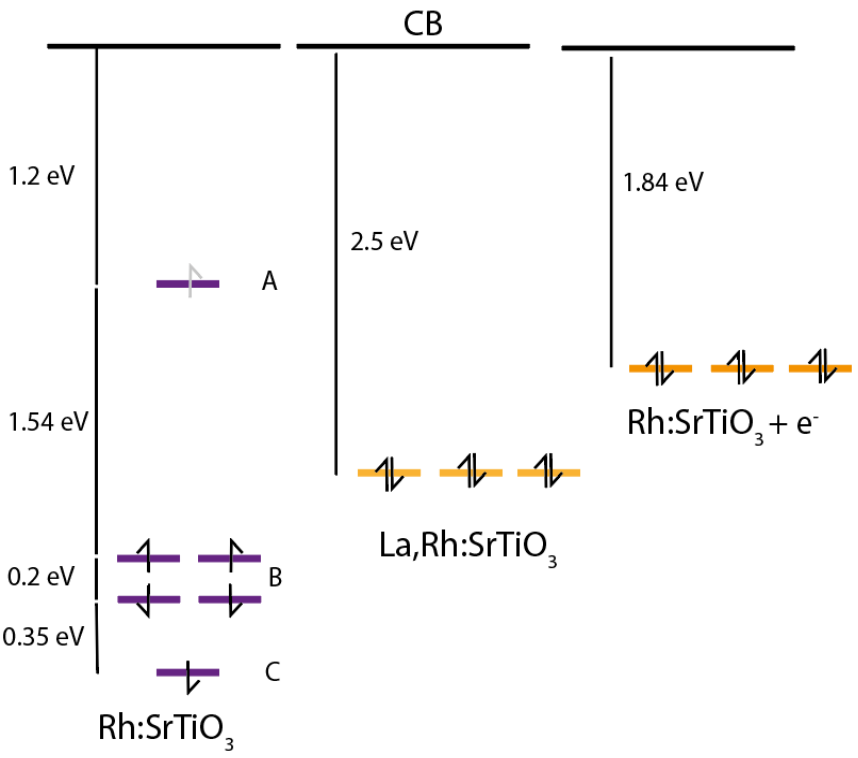

Figure S6.2. **Rh 4d spin polarised electron count** near the Fermi level of $Rh:SrTiO_3$, $La,Rh:SrTiO_3$ and $Rh:SrTiO_3$ in the presence of a compensating background charge ($Rh:SrTiO_3 + e^-$). The grey state (A) indicates the spin of a Rh 4d vacant state.

Splitting of the Rh 4d dopant states responsible for visible light harvesting.

Figure S6.2 shows the results of integrating the spin polarised partial density of states projecting onto Rh 4d orbitals near the effective valence band edge. It is apparent from this figure that the electronic structure of the Rh 4d orbital of $Rh:SrTiO_3$ is distinct from $La,Rh:SrTiO_3$ in several aspects. Firstly, filled Rh states do not appear to be degenerate but rather show two distinct peaks – an overlapping set of spin up and down states just beneath the Fermi level (labelled B) and a single spin down state 0.55 eV beneath the Fermi level (C). Secondly, a vacant mid gap level is present 1.5 eV above the Fermi level (labelled A). In contrast, $La,Rh:SrTiO_3$ shows a single set of filled states just beneath the Fermi level. In two of the Rh 4d orbitals in $Rh:SrTiO_3$ (B), non-degeneracy of spin states appears to be relatively minor, with a splitting of 0.2 eV distinguishing spin up and spin down states. However, in the half-filled orbital, the effect is significantly more pronounced, leading to a gap of over 1.8 eV between the filled spin down state (C) and the vacant spin up state (A, see following figure for the link between orbital A and C). Intriguingly this splitting is not symmetric *i.e.* the up and down spin states do not appear 1.8/2=0.9 eV above and below the other orbitals labelled B. Rather, the vacant spin up state appears to be destabilised more than the spin down state is stabilised. Confirmation that this effect is related to Rh reduction rather than interaction with La can be found by adding an electron in the presence of compensating background charge. Addition of an electron to the supercell in the presence of a compensating background charge ($Rh:SrTiO_3 + e^-$) results in the localisation of the electron on the Rh 4d shell upon optimisation and the reorganisation of the 4d orbitals to form a triply degenerate set, as in $La,Rh:SrTIO_3$.

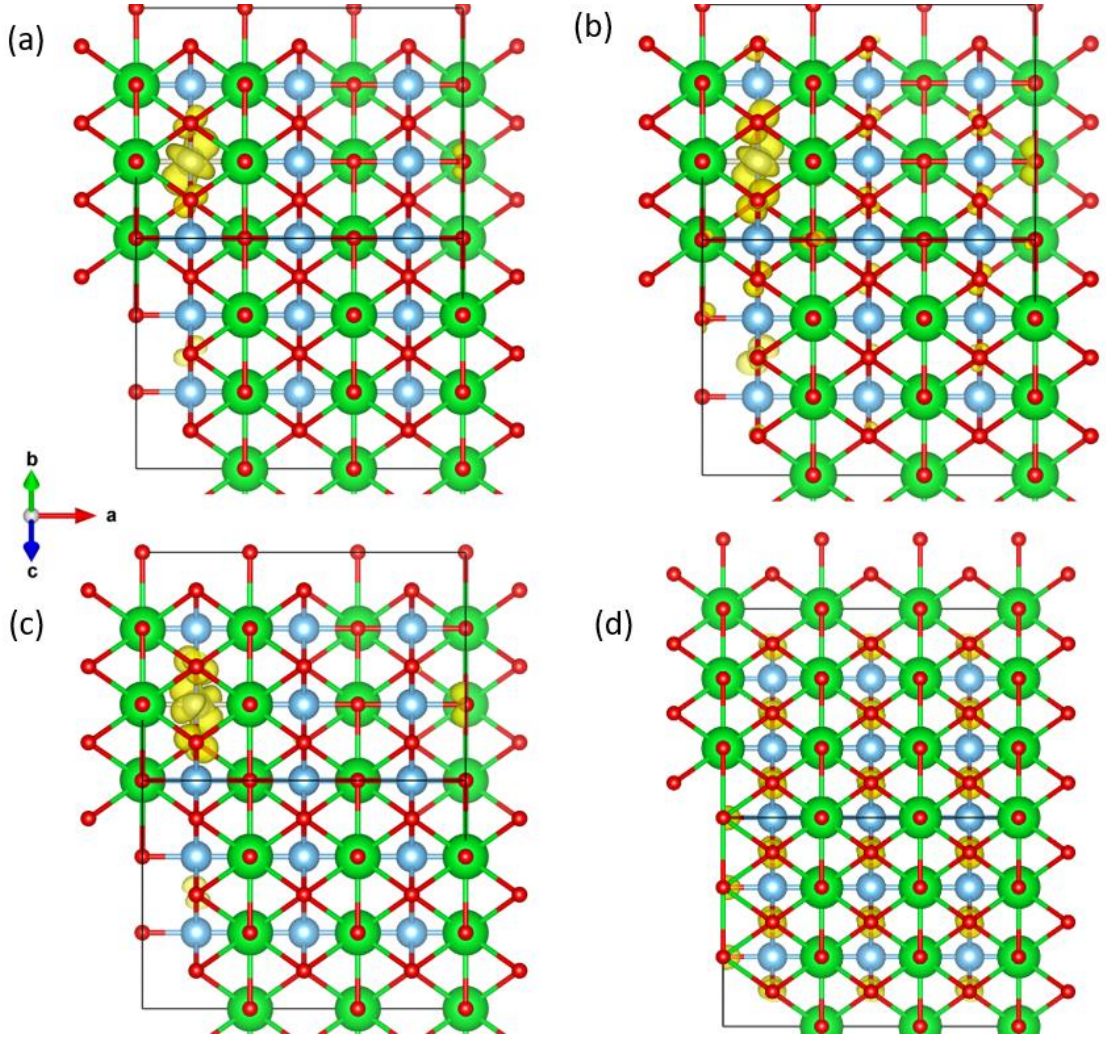

Figure S6.3. **Iso-surfaces of the Rh 4d states situated above the valence band of $SrTiO_3$** (responsible for visible light absorption). (a) An example of the lowest energy filled Rh state observed in Rh:$SrTiO_3$ (C in Fig.S6.2). (b) An example of the vacant mid gap state observed in Rh:$SrTiO_3$ (A in Fig. S6.2). (c) An example of a localised state at the effective VB edge observed in all doped materials (d) an example of a typical O2p valence band state in $SrTiO_3$ showing a high degree of delocalisation.

Visualisation of the Rh 4d dopant states responsible for visible light harvesting.

Figure S6.3a and 3b shows visualisations of typical orbitals from the density of states in the region labelled A and C in Figure S6.2, respectively. We note that it appears that A and C are related, as both apparently exhibit the characteristic shape of Rh 4d z^2 orbitals. However, the stabilised state (C) exhibits significant delocalisation across the lattice. Whilst the vacant mid-gap state (A) appears to be strongly localised around the Rh and neighbouring oxygens. From this we tentatively suggest that an interaction of the lattice with the RhO_6 dopant cluster may be giving rise to this effect. A detailed investigation is beyond the scope of this work, but merits further study. In oxidised and reduced materials, the states just beneath the Fermi level appear to be strongly localised– a typical example is visualised (Fig. S6.3c). For comparison a highly delocalised O2p state from the valence band of undoped $SrTiO_3$ is shown in (Fig S6.3d).

Band alignment

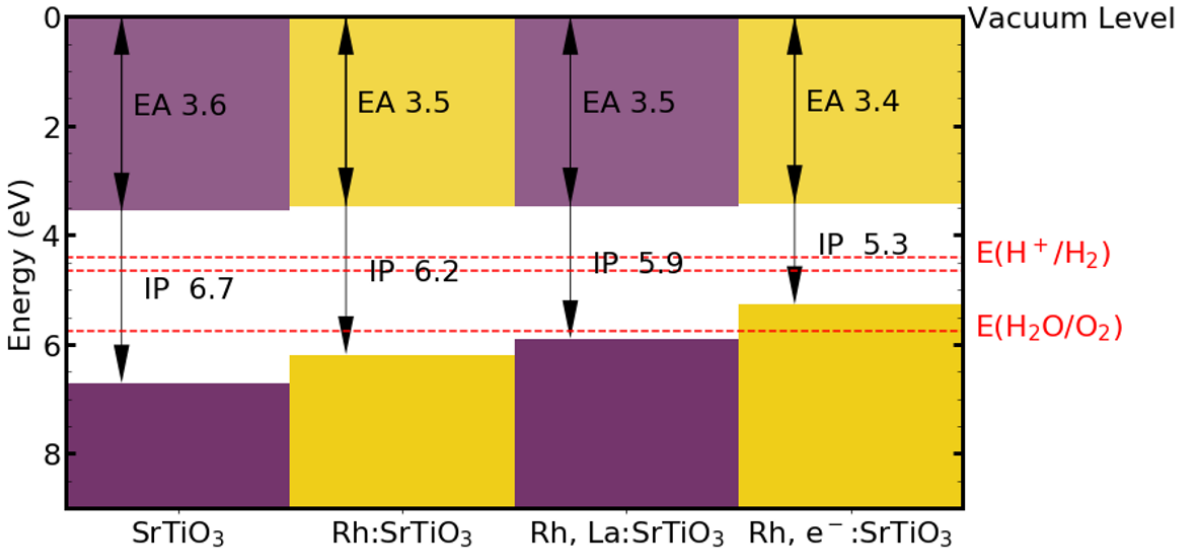

Figure S6.4 **Calculated band alignment** of $Rh:SrTiO_3$, $La,Rh:SrTiO_3$ and $Rh:SrTiO_3$ in the presence of a compensating background charge ($Rh:SrTiO_3 + e^-$). EA and IP stands for electron affinity and ionization potential, respectively.

Figure S6.4 compares the energy level alignment of $SrTiO_3$ to $Rh:SrTiO_3$ and $La,Rh:SrTiO_3$, achieved by aligning the orbitals of $SrTiO_3$ to the vacuum. Doped $SrTiO_3$ orbitals are then aligned through the alignment of oxygen core levels to that of $SrTiO_3$. This shows that upon doping, only minor changes in the position of the condition band are observed. In contrast, a 0.4 eV shift in the energy of the highest occupied state is observed upon Rh doping, with a further 0.2 eV shift to higher energy upon La co-doping. This is consistent with the shift of Rh 4d orbitals to higher energy upon reduction of Rh. Further confirmation that Rh reduction is responsible for this effect can be obtained by adding an electron to $Rh:SrTiO_3$ in the presence of a compensating background charge. Here, the added electron was found to localise on (i.e. reduce) Rh^{4+} again leading to a shift in the energy of the highest occupied state to higher energy without strongly affecting the energy of the condition band edge, which does not exhibit Rh d character.

Effect of increased Rh concentration.

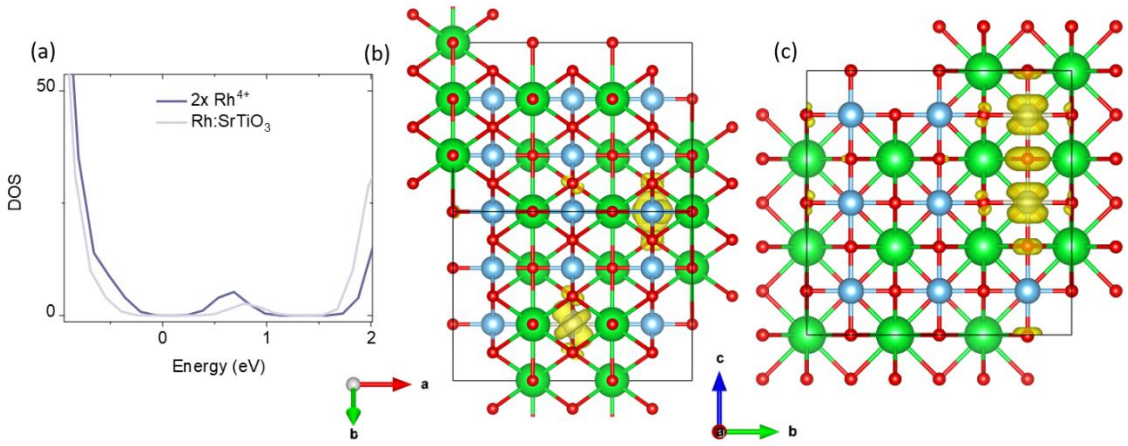

Figure S6.5. **Effect of increased Rh concentration** (a) Calculated DOS of typical Rh state iso surface of doubly doped $Rh:SrTiO_3$. Iso surfaces of next nearest (b) and nearest (c) neighbour doping configurations which exhibit a commensurate degree of localisation.

Rh:$SrTiO_3$ exhibits surface segregation of Rh, leading to higher than nominal Rh concentrations than the nominal doping density at its surface. To explore the effect of increasing Rh density, and in particular the possibility of interaction between Rh states we calculated the electronic structure of all non-symmetry equivalent configurations of a doubly doped Rh:$SrTiO_3$ super cell. These show no qualitative and little quantitative differences as no new states are observed with only an increased DOS (from higher [Rh]) occurring alongside a minor shift in energy (Fig S6.5a). Only when dopants are in nearest-neighbour positions does the degree of localization of the gap state (not its energy) change slightly. Here, the empty gap states are still mainly located on the Rh centres, but somewhat more delocalized to partially involve the shared oxygen anion too (Fig. S6.5b,c). Thus, even in the pairing case the interaction is weak and has little effect on the electronic structure. The energy position of the empty gap state is therefore largely independent of the relative position of the Rh dopants, suggesting no strong interaction between RhO_6 octahedra. Furthermore, dopant pairing is found to be energetically unfavourable (by ~0.14 eV with respect to a distant Rh-Rh pair). That means, for example, that at 7.4 mol% Rh doping and room temperature, the probability of a Rh dopant to be a nearest neighbour of another Rh dopant is less than 1 in 300 at thermodynamic equilibrium. This provides further justification to conclude that Rh states are mostly localised at Rh centres, even when Rh is segregated at the surface.

S7. Photovoltage measurements

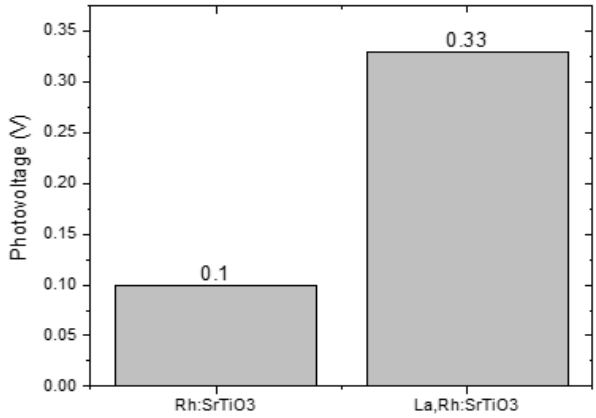

Figure S7. **Photovoltage measurements.** Comparison of photovoltage generated by (La),Rh:$SrTiO_3$ sheets from illumination with 4 mW cm^{-2} of 400 nm light for 150 s.

References:

1. Wang, Q. *et al.* Scalable water splitting on particulate photocatalyst sheets with a solar-to-hydrogen energy conversion efficiency exceeding 1%. *Nat. Mater.* **15**, 611–615 (2016).

2. Wang, Q. *et al.* Particulate photocatalyst sheets based on carbon conductor layer for efficient Z-scheme pure-water splitting at ambient pressure. *J. Am. Chem. Soc.* **139**, 1675–1683 (2017).

3. Kresse, G. & Joubert, D. *From ultrasoft pseudopotentials to the projector augmented-wave method*.

4. Perdew, J. P. *et al.* Generalized gradient approximation for solids and their surfaces. (2007). doi:10.1103/PhysRevLett.100.136406

5. Kresse, G. & Furthmüller, J. Efficient iterative schemes for ab initio total-energy calculations using a plane-wave basis set. *Phys. Rev. B - Condens. Matter Mater. Phys.* **54**, 11169–11186 (1996).

6. Moreno, J. & Soler, J. M. Optimal meshes for integrals in real- and reciprocal-space unit cells. *Phys. Rev. B* **45**, 13891–13898 (1992).

7. Godin, R., Wang, Y., Zwijnenburg, M. A., Tang, J. & Durrant, J. R. Time-Resolved Spectroscopic Investigation of Charge Trapping in Carbon Nitrides Photocatalysts for Hydrogen Generation. *J. Am. Chem. Soc.* **139**, 5216–5224 (2017).

8. Wilkinson, F. Diffuse reflectance laser flash photolysis. *J. Photochem.* **17**, 52 (1981).

9. Kessler, R. W., Oelkrug, D. & Wilkinson, F. *The Detection of Transient Spectra within Polycrystalline Samples Using the New Technique of Diffuse Reflectance Flash Photolysis*.

10. Chen, Z., Dinh, H. N. & Miller, E. *Photoelectrochemical Water Splitting*. (Springer, 2013).

11. Gelius, U. *et al.* Molecular Spectroscopy by Means of ESCA III. Carbon compounds. *Phys. Scr.* **2**, 70–80

12. Nagarkar, P. V, Searson, P. C. & Gealy, F. D. Effect of surface treatment on SrTiO 3 : An x-ray photoelectron spectroscopic study. *J. Appl. Phys.* **69**, 459 (1991).

13. Nono Tchiomo, A. P., Babu-Geetha, G., Carleschi, E., Ngabonziza, P. & Doyle, B. P. Surface characterization of clean SrTiO 3 (100) substrates by x-ray photoelectron spectroscopy. *Surf. Sci. Spectra* **25**, 024001 (2018).

14. Dupin, J.-C., Gonbeau, D., Vinatier, P. & Levasseur, A. Systematic XPS studies of metal oxides , hydroxides and peroxides. *Phys. Chem. Chem. Phys.* **2**, 1319–1324 (2000).

15. Wang, Q., Hisatomi, T., Ma, S. S. K., Li, Y. & Domen, K. Core/shell structured La- and Rh-Codoped SrTiO3 as a hydrogen evolution photocatalyst in Z-scheme overall water splitting under visible light irradiation. *Chem. Mater.* **26**, 4144–4150 (2014).

16. Glover, E. N. K., Ellington, S. G., Sankar, G. & Palgrave, R. G. The nature and effects of rhodium and antimony dopants on the electronic structure of TiO_2: Towards design of Z-scheme photocatalysts. *J. Mater. Chem. A* **4**, 6946–6954 (2016).

17. Oropeza, F. E. & Egdell, R. G. Control of valence states in Rh-doped TiO2 by Sb co-doping: A study by high resolution X-ray photoemission spectroscopy. *Chem. Phys. Lett.* **515**, 249–253 (2011).

18. Kawasaki, S. *et al.* Epitaxial Rh-doped SrTiO3 thin film photocathode for water splitting under visible light irradiation. *Appl. Phys. Lett.* **101**, 033910 (2012).